

Trained Uniform Quantization for Accurate and Efficient Neural Network Inference on Fixed-Point Hardware

Sambhav R. Jain⁺* Albert Gural^{†*} Michael Wu⁺ Chris Dick⁺

⁺Xilinx Inc. [†]Stanford University

{sambhav, agural}@alumni.stanford.edu {miwu, chrisd}@xilinx.com

Abstract

We propose a method of training quantization clipping thresholds for uniform symmetric quantizers using standard backpropagation and gradient descent. Our quantizers are constrained to use power-of-2 scale-factors and per-tensor scaling for weights and activations. These constraints make our methods better suited for hardware implementations. Training with these difficult constraints is enabled by a combination of three techniques: using accurate threshold gradients to achieve range-precision trade-off, training thresholds in log-domain, and training with an adaptive gradient optimizer. We refer to this collection of techniques as *Adaptive-Gradient Log-domain Threshold Training (ALT)*. We present analytical support for the general robustness of our methods and empirically validate them on various CNNs for ImageNet classification. We are able to achieve floating-point or near-floating-point accuracy on traditionally difficult networks such as MobileNets in less than 5 epochs of quantized (8-bit) retraining. Finally, we present *Graffitist*, a framework that enables immediate quantization of TensorFlow graphs using our methods. Code available at <https://github.com/Xilinx/graffitist>.

1. Introduction

Machine learning continues to be increasingly pervasive in applications that span the cloud to the edge. Low-precision quantization, such as uniform quantization between two clipping thresholds, is an important technique enabling low-power, high-throughput implementations and a mechanism for managing memory bandwidth requirements in neural network inference. However, this reduced precision leads to commensurate reductions in accuracy.

Retraining weights with quantization-in-the-loop is a useful technique to regain some lost accuracy. However the quantization thresholds are typically fixed after initial calibration, causing (a) lack of ability to adapt to chang-

ing weight and activation distributions during training, and (b) threshold calibration based on local quantization errors that is agnostic to global neural network loss. We address both of these issues by treating thresholds as learnable parameters whose gradients can be computed through backpropagation and adjusted via gradient descent. Therefore, (a) our thresholds can be trained along with weights during quantized training, and (b) the gradients are computed on the overall loss meaning the learned thresholds are more optimal for the network as a whole.

The idea of learning clipping thresholds via gradient descent is not completely novel. For example, TensorFlow [1, 2] defines gradients with respect to min/max variables in their FakeQuant implementation [35, 34]. However, when computing the gradients they appear to bypass the round function even during forward pass evaluation, which has the mathematical effect of causing the thresholds to train to the minimum and maximum of the input distribution, rather than finding a good range-precision trade-off point. We discuss this in detail in Section 3.5. Only very recently (and independently of our work), others have published work [9] showing the need to keep the round function in the forward pass. We discuss this work at the end of Section 2.

Besides the general method to train quantization thresholds using accurate gradients discussed in Section 3, our work presents several other novel contributions. To our knowledge, it is the first work to demonstrate quantization threshold training with per-tensor and power-of-2 scaling constraints. These are practically useful limitations for maximizing hardware efficiency. To achieve this, we provide an easy-to-implement and fast convergence training scheme (ALT) that only requires training thresholds in the log-domain using an adaptive gradient optimizer. We demonstrate that our implementation and hyperparameter recommendations are robust, analytically in Section 4 and empirically in Section 6. Additionally, in Section 5 we present a framework for automatic quantization of TensorFlow graphs using our methods. Finally we discuss insights from ALT training in Section 7.

*equal contribution

2. Related Work

The push to reduce power consumption for inference on the edge and improve throughput and/or latency for inference on the cloud has motivated strong interest in neural network quantization research in just the past few years.

Historically, some of the earlier work in quantization looked at low bit-width weights, and in some cases, activations. BinaryNet [7] proposed quantizing weights and activations to binary values of +1 and -1 and showed that weights could be trained using a straight-through estimator (STE) [4], where quantization is applied in the forward pass but approximated to a clipped identity function in the backward pass. XNOR-Nets [26] uses a different network and binarization method with scale-factors based on the maximum per-channel activation values, to achieve better ImageNet performance. Ternary networks [22, 41] add another quantization level at 0 suggesting this helps significantly with accuracy. TTQ [41] also suggest using a codebook to map the two non-zero quantization levels to arbitrary values that can be trained with gradient descent by averaging the gradients of the weights within each quantization bucket.

Continuing the trend for higher accuracy, researchers revisited multi-bit quantization. Initially, the quantization range tended to be fixed, such as in DoReFa-Net [40] where elements are limited to [-1, 1] with the tanh function, or WRPN [25] which limits weights to [-1, 1] and activations to [0, 1] even during floating point training. To improve accuracy further, researchers considered non-fixed quantization ranges. HWGQ [5] uses ReLU activation and learns a clipping range by minimizing L2 loss of pre- and post-quantized values. PACT [6] learns this ReLU clipping parameter α through gradient descent, using the gradient

$$\frac{\partial y_q(x; \alpha)}{\partial \alpha} = \begin{cases} 0 & x \in (-\infty, \alpha) \\ 1 & x \in [\alpha, +\infty) \end{cases} \quad (1)$$

derived using the STE. LQ-Nets [39] achieve state-of-the-art accuracy through a custom quantization error minimization (QEM) algorithm and non-uniform quantization scheme with decision levels derived from a small binary encoding basis. QIL [19] likewise introduces a custom quantization scheme based on trainable quantization intervals.

While more extravagant quantization schemes can be used to push accuracy to the limit, simpler more realistic hardware-aware quantization schemes are becoming increasingly promising in the industry. NVIDIA’s TensorRT [24] proposed an 8-bit symmetric uniform per-tensor quantization with statically calibrated thresholds. They demonstrate the range-precision trade-off through local Kullback-Leibler (KL) divergence minimization and show good performance for traditional CNNs but do not explore retraining. Google’s TensorFlow Lite supports quantization-aware training [37] which is based on previous work [18] using

asymmetric uniform quantization. They demonstrate learning the clipping thresholds through an exponential moving average of the min/max values of the input distributions seen during initial warm-ups on random batches of training data. This is consistent with their gradient definition [35] which does not allow for a range-precision trade-off, as seen from the quantizer transfer curves in Section 3.5. Google’s whitepaper [21] reviews the commercially relevant quantization schemes and design choices such as affine or symmetric uniform quantization, per-tensor or per-channel scaling, and batch normalization [15] considerations for quantization-aware training. IBM’s FAQ [23] uses percentile initialization to the 99.99th percentile for 8-bit and 99.9th percentile for 4-bit for determining clipping thresholds, but does not train these thresholds.

FAT [10] does propose training the quantization thresholds through gradient descent while keeping the weights unchanged. They use an unlabeled dataset and train on a root-mean-square-error loss between the original and quantized networks. NICE [3] starts with a clamping parameter c_a located α standard deviations from the mean of the input distribution, and trains it using gradient descent on a derivative found using the STE in a formulation similar to (1).

Independently of our work, IBM’s LSQ [9] found very similar gradient definition for the quantizer and uses back-propagation to train them. However, our works differ in several interesting ways. For example, they learn the scale-factors directly and do not restrict them to power-of-2. Besides the evident implications for accuracy and hardware implementation, we show in Section 4 that this also has major implications for training stability due to scale dependence of learning rate. As a workaround to these stability issues, they require careful fine-tuning of hyperparameters and consequently retrain for 90 epochs compared to 5 epochs in our case. They also use high precision in the first and last layers to retain performance, as is common in the field. We suspect the high precision and lack of power-of-2 limitations allow for very high accuracy in their low bit-width experiments. Further, they do not explore quantization on more difficult networks such as MobileNets [14, 29]. We address these issues with a different gradient formulation in Section 3 and justify it analytically in Section 4.

3. Trained Uniform Quantization

3.1. Quantization Scheme

A simple design choice for a uniform quantizer is one that uses an affine mapping between the real domain r and the quantized domain q , such as

$$r = s \cdot (q - z) \quad (2)$$

where constants s (scale-factor) and z (zero-point) are the quantization parameters. Generally, s is a positive real num-

ber, and z is a quantized value that maps to the real zero¹.

While the affine quantizer allows for a direct mapping from floating point values to integers (without the need for lookup tables), there is added cost due to special handling of zero-points and real-valued scale-factors (see Appendix A).

For efficient implementation on fixed-point hardware, we constrain our quantization scheme to use:

1. **No zero-points:** By setting $z = 0$, the affine quantizer in (2) reduces to a symmetric quantizer:

$$r = s \cdot q \quad (3)$$

This allows us to drop cross-terms that otherwise arise from a matrix multiplication or convolution operation involving zero-points (see Appendix A.1). A natural consequence is that symmetric quantization can be less precise with highly asymmetric or skewed distributions.

2. **Power-of-2 scale-factors:** Instead of allowing real-valued scale-factors, we constrain them to the form $s = 2^{-f}$ (where f is an integer denoting the fractional length; f can be positive or negative). This enables scaling using simple bit-shifts without the overhead of a fixed-point multiplier operation (see Appendix A.2). Right bit-shifts get round to the nearest integer, with round-half-to-even to prevent bias.
3. **Per-tensor quantization:** Elements in a given weight or activation tensor are quantized using a single scale-factor s , commonly referred to as per-tensor quantization. While it is common practice to use per-channel quantization for networks with depthwise convolutions such as MobileNets, we find that per-tensor combined with ALT training works well for INT8, and that per-channel may only be necessary for such networks at lower bit-widths (e.g., INT4).
4. **Mid-tread quantizer:** In BinaryNet [7], weights and activations are quantized to +1 and -1 using a mid-rise quantization scheme based on a classification threshold at 0. As a result, 0 is not representable in the quantized domain. In contrast, vanilla hardware multipliers accept 0 as a valid input, so a quantization scheme which includes 0 in its quantized domain is more natural and makes better use of existing hardware. Therefore, we restrict our quantizers to mid-tread with classification thresholds at integers + 0.5.

3.2. Linear Quantizer - Forward Pass

Having constrained our uniform quantizer to use linear mapping with no zero-points, power-of-2 scale-factors, per-

¹This formulation satisfies the domain specific constraint (with neural networks and zero padding) that the real zero be exactly representable in the quantized domain [16, 18, 21].

tensor and mid-tread quantization, we can proceed to define its forward pass characteristics.

The quantization function $q(x; s)$ for a tensor x is parameterized only by its scale-factor s , which depends on threshold t and bit-width b chosen for this tensor². $q(x; s)$ performs quantization by applying four point-wise operations (in order): scale, round, saturate and de-quant, each of which is explained below.

Scale: Tensor elements are scaled such that the lowest power-of-2 larger than raw threshold t (i.e., $2^{\lceil \log_2(t) \rceil}$, where $\lceil \cdot \rceil$ denotes ceil³) is mapped to the largest value supported in the quantized domain (i.e., 2^{b-1} if signed, or 2^b if unsigned). Naturally, elements that fall out of the saturation threshold $2^{\lceil \log_2(t) \rceil}$ in either direction would be clipped.

Round: The scaled tensor elements are round to nearest integers using bankers rounding (round-half-to-even) denoted by $\lfloor \cdot \rfloor$ in the equations below. This prevents an overall upward or downward bias which is known to impact end-to-end inference accuracy in neural networks [18].

Saturate: Once scaled and rounded, it is possible for some elements in the tensor to have exceeded the largest value supported in the quantized domain; such elements are clipped: $\text{clip}(x; n, p) = \min(\max(x, n), p)$. Since we apply clipping to the scaled tensor, the clipping limits (n, p) are constants independent of the real bounds. If the tensor is signed, we clip to $(-2^{b-1}, 2^{b-1} - 1)$ and if unsigned, we clip to $(0, 2^b - 1)$.

De-quant: The last step undoes the scaling step. Therefore, we emulate the effect of quantization while retaining the original scale of the input tensor.

Putting together the point-wise operations from above, the quantization function $q(x; s)$ can be formally written as:

$$q(x; s) := \text{clip}\left(\left\lfloor \frac{x}{s} \right\rfloor; n, p\right) \cdot s, \quad (4)$$

where $n = -2^{b-1}$, $p = 2^{b-1} - 1$ and $s = \frac{2^{\lceil \log_2 t \rceil}}{2^{b-1}}$ for signed data; $n = 0$, $p = 2^b - 1$ and $s = \frac{2^{\lceil \log_2 t \rceil}}{2^b}$ for unsigned data.

3.3. Linear Quantizer - Backward Pass

In the backward pass we can use gradient descent to simultaneously update quantization thresholds and weights of the quantized network. To do this, we derive the local gradients of our quantizer $q(x; s)$ with respect to scale-factor s and input x . By formulating the quantization function in (4) to perform clipping after scaling, the clipping limits (n, p) are constants independent of s . Further, we (carefully) use the STE to approximate gradients of round/ceil to 1, with

²While we fix b for each tensor (at compile time) based on the footprint of the fixed-point hardware it maps to (albeit configurable), we allow t (hence s) to be trained using backpropagation.

³The ceil function ensures a power-of-2 scale-factor that is initially biased in the direction of having more elements within the clipping range.

out approximating round/ceil to be identity. Specifically, we define $\frac{\partial}{\partial x} \lfloor x \rfloor = \frac{\partial}{\partial x} \lceil x \rceil = 1$, but $\lfloor x \rfloor \neq x$ and $\lceil x \rceil \neq x$.

Considering the three cases of how $\lfloor \frac{x}{s} \rfloor$ compares to n and p , we re-write (4) as:

$$q(x; s) := \begin{cases} \lfloor \frac{x}{s} \rfloor \cdot s & \text{if } n \leq \lfloor \frac{x}{s} \rfloor \leq p, \\ n \cdot s & \text{if } \lfloor \frac{x}{s} \rfloor < n, \\ p \cdot s & \text{if } \lfloor \frac{x}{s} \rfloor > p. \end{cases} \quad (5)$$

The local gradient with respect to scale-factor s is:

$$\nabla_s q(x; s) := \begin{cases} \lfloor \frac{x}{s} \rfloor - \frac{x}{s} & \text{if } n \leq \lfloor \frac{x}{s} \rfloor \leq p, \\ n & \text{if } \lfloor \frac{x}{s} \rfloor < n, \\ p & \text{if } \lfloor \frac{x}{s} \rfloor > p. \end{cases} \quad (6)$$

Noting that $\nabla_{(\log_2 t)} s = s \ln(2)$,

$$\nabla_{(\log_2 t)} q(x; s) := s \ln(2) \cdot \begin{cases} \lfloor \frac{x}{s} \rfloor - \frac{x}{s} & \text{if } n \leq \lfloor \frac{x}{s} \rfloor \leq p, \\ n & \text{if } \lfloor \frac{x}{s} \rfloor < n, \\ p & \text{if } \lfloor \frac{x}{s} \rfloor > p \end{cases} \quad (7)$$

The choice to train thresholds in the log-domain is simple yet very effective for various stability reasons discussed in Section 4.

Similarly, the local gradient with respect to input x is:

$$\nabla_x q(x; s) := \begin{cases} 1 & \text{if } n \leq \lfloor \frac{x}{s} \rfloor \leq p, \\ 0 & \text{otherwise} \end{cases} \quad (8)$$

3.4. Interpretation of Gradients

To qualitatively understand the role of threshold gradient $\nabla_{(\log_2 t)} q(x; s)$ and input gradient $\nabla_x q(x; s)$ during backpropagation, let us consider the following toy problem: A single quantizer optimized using least-square-error loss $L = (q(x; s) - x)^2 / 2$. The overall gradients of L are:

$$\nabla_{(\log_2 t)} L = (q(x; s) - x) \cdot \nabla_{(\log_2 t)} q(x; s) \quad (9)$$

$$\nabla_x L = (q(x; s) - x) \cdot (\nabla_x q(x; s) - 1) \quad (10)$$

Figure 1 shows the forward and backward pass transfer curves for our quantizer. As noted, the exact clipping thresholds of x in the real domain are $x_n = s \cdot (n - 0.5)$ and $x_p = s \cdot (p + 0.5)$.

Role of threshold gradients: As seen from the plots of $\nabla_{(\log_2 t)} L$ vs. x in Figure 2, threshold gradients are positive for x within clipping thresholds (x_n, x_p) and negative otherwise. When most of the input distribution falls within (x_n, x_p) , the cumulative threshold gradient is positive causing $\log_2 t$ to decrease⁵. In other words, the limits (x_n, x_p) get pulled inward in favor of larger precision.

⁴Gaussian distributed in this example, but the analysis holds in general.

⁵From the update rule $\log_2 t := \log_2 t - \alpha \nabla_{(\log_2 t)} L$ where α is the learning rate.

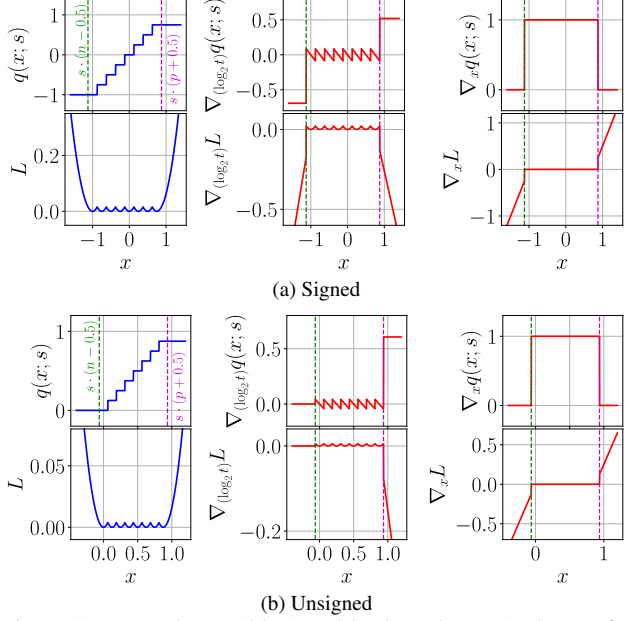


Figure 1. Forward pass (blue) and backward pass (red) transfer curves of our quantizer for signed and unsigned data. Local gradients shown in the top rows, and overall gradients of L_2 -loss in the bottom rows. We pick bit-width $b = 3$ and raw threshold $t = 1.0$ in this example.

Similarly, when most of the input distribution falls outside (x_n, x_p) , the cumulative threshold gradient is negative, $\log_2 t$ increases, and the limits (x_n, x_p) get pushed outward in favor of larger dynamic range. This technique is naturally robust to ill-behaved distributions (e.g., long tails or outliers) by achieving range-precision trade-off through gradient-based optimization.

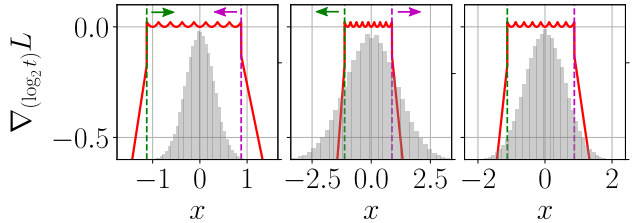


Figure 2. Trained thresholds move inward (left) or outward (center) to achieve range-precision trade-off. When converged (right), the positive gradients from x within (x_n, x_p) cancel the negative gradients from x outside (x_n, x_p) .

Role of Input Gradients: Using a similar analysis as for threshold gradients, we see that the input gradients $\nabla_x L$ are non-zero for values of x that fall outside (x_n, x_p) , biased to keep them from getting clipped. This encourages the weight and activation distributions to be tighter.

To summarize, threshold gradients help train optimal thresholds for clipping weights and activations, whereas in-

put gradients nudge the weights and activations to tighter bounds. By simultaneously training clipping thresholds and weights of the quantized network through backpropagation, we adopt joint (mutual) optimization over a global loss. While the actual loss landscape is non-trivial, the qualitative analysis from our toy problem still holds.

3.5. Comparison to Clipped Threshold Gradients

In contrast, we find quantizer implementations that define threshold gradients by simply clipping the upstream gradients at the saturation thresholds. For example TensorFlow’s FakeQuant (used for quantization-aware training [37, 18]) defines gradients with respect to min/max thresholds as a clip function (see kernel implementation [35]).

In the forward pass, TF-FakeQuant operation [34] is mathematically equivalent to our formulation (except with zero-point), defined as:

$$q(x; n, p) := \left\lfloor \frac{\text{clip}(x; n, p) - n}{\frac{p - n}{2^b - 1}} \right\rfloor \cdot \frac{p - n}{2^b - 1} + n, \quad (11)$$

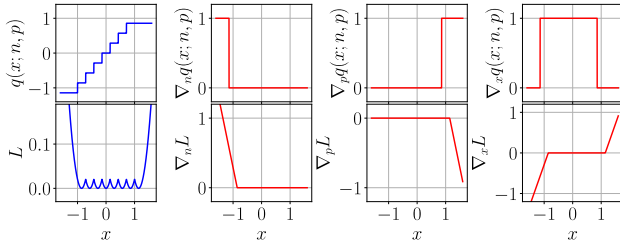


Figure 3. Forward pass (blue) and backward pass (red) transfer curves of TF-FakeQuant for signed data. Local gradients shown in the top rows, and overall gradients of L_2 -loss in the bottom rows. We pick bit-width $b = 3$ and clipping thresholds $n = -1.125, p = 0.875$ to match with our example.

However, in the backward pass they likely treat the round function to be identity in (11), reducing it to a clip function with clipped gradients. This is consistent with the TF-FakeQuant transfer curves in Figure 3 showing that the gradients with respect to thresholds (n, p) are trivially clipped to zero for x within (n, p) . In other words, the cumulative gradients always push the limits (n, p) outward, thus training to the actual min/max of the input distributions and favoring range at the cost of precision. This is particularly bad for distributions with long tails or outliers because the scheme discourages clipping.

4. Log Threshold Training

Initially, it may seem that with the definition of a gradient with respect to the raw threshold, backpropagation and gradient descent could be immediately used to train it. How-

ever, just as training weights in a vanilla neural network requires care in the choice of optimizer and learning rate, here too care must be taken to ensure training stability and convergence. There are three main properties we would like our training procedure to satisfy: numerical stability, scale invariance, and convergence. Here we discuss each of these issues and the engineering tweaks used to solve them.

4.1. Numerical Stability

One obvious problem with training raw thresholds $t \in \mathbb{R}^+$ is that gradient updates could potentially bump a threshold to a negative value, causing $\log_2 t$ and therefore scale-factor s to diverge. If this happens even once, the network as a whole will break. An easy solution is to train $\log_2 t$ as opposed to t itself, since its domain is $\log_2 t \in \mathbb{R}$. Using log thresholds is convenient because it already appears in the expression for $s(t)$. However, the most important benefit is described in Section 4.2, where the log representation makes ensuring scale invariance very easy.

4.2. Scale Invariance

For a given input distribution we prefer that the threshold gradients have similar magnitudes regardless of the position of the threshold itself. This *threshold scale invariance* is useful for making sure training is not too slow when the thresholds are far from their optimal values. Similarly, the properties of our threshold gradients should not depend on the scale of the input distribution. This *input scale invariance* is important because it ensures that quantized training behaves the same way for the different weights and activations in the network, even if the variance of their distributions vary over many orders of magnitude.

Unfortunately, neither of these scale invariances hold. Far from improving, Figure 4 shows that in moving from raw threshold training (left) to log threshold training (middle), both scale invariance properties of the threshold gradients actually degrade.

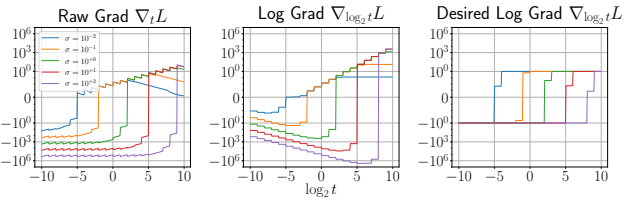


Figure 4. Gradients of L_2 -loss with respect to raw threshold (left) or log threshold (middle, right) versus log threshold, for Gaussian(σ) inputs of varying σ . Desired (normed) gradients for the log threshold case are shown on the right.

Threshold scale invariance: Updates to the log threshold would be threshold scale invariant if the gradients on both sides of the negative-to-positive jump were flat, as seen in the right plot of Figure 4. However, this is not the case

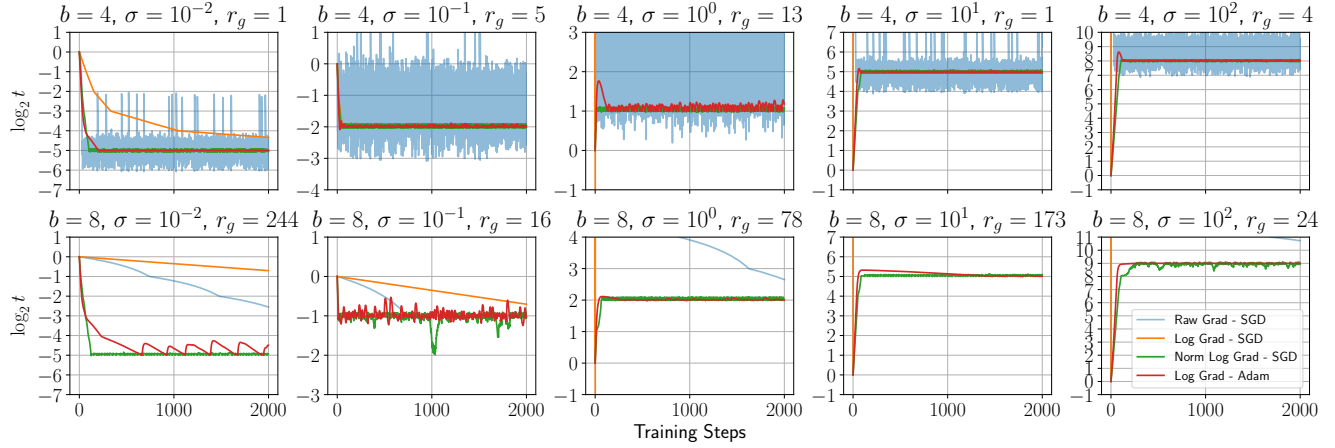


Figure 5. Raw, log and normed log threshold training on L_2 -loss for 2000 steps with learning rate $\alpha = 0.1$. We compare different bit-widths - 4 (top) and 8 (bottom), and Gaussian(σ) inputs of varying σ - smallest (left) to largest (right). The empirical value of r_g is estimated from the last few hundred steps of Adam.

for log threshold gradients (center plot of Figure 4). On the left-of-jump side, as $\log_2 t$ decreases, gradients of (hence updates to) $\log_2 t$ get exponentially smaller, meaning it will converge very slowly to lower optimal values (see the log grad SGD case in the left plots of Figure 5). Similarly, on the right-of-jump side, as $\log_2 t$ increases, updates to $\log_2 t$ increase exponentially, meaning it will converge very quickly and possibly unstably to higher optimal values (see the log grad SGD case in the right plots of Figure 5). In the raw threshold domain, we would like gradients of (hence updates to) t to scale proportional to t . This is also not the case for the left-of-jump side of raw threshold gradients (left plot of Figure 4). In other words, the raw and log threshold gradients are swapped from what we would prefer on the left-of-jump sides.

Input scale invariance: Updates to the log threshold are input scale invariant if the gradients are threshold scale invariant and x-axis shifted copies for varying input scales, as seen in the right plot of Figure 4. However, this is not the case for log threshold gradients (center plot of Figure 4) as the gradient magnitudes depend on the scale of the input. In fact when accounting for the threshold scale dependence, the gradient magnitudes depend quadratically on the scale of the input.

Normed gradients: While neither raw or log threshold gradients have the desired properties of scale invariance, only minimal modifications to our log threshold gradient is needed to get these properties to hold (see desired log threshold gradient on the right of Figure 4). In particular, if we normalize the gradient g_i by its bias-corrected moving average variance, we achieve a close approximation of the desired gradients \tilde{g}_i (12). To improve stability, we can encapsulate (12) in a clipping function to guarantee no large gradients (13).

$$v_i \leftarrow \beta v_{i-1} + (1 - \beta) g_i^2 \quad (12)$$

$$\hat{v}_i \leftarrow \frac{v_i}{1 - \beta^i} \quad (12)$$

$$\tilde{g}_i \leftarrow \frac{g_i}{\sqrt{\hat{v}_i} + \epsilon} \quad (12)$$

$$\tilde{g}_i \leftarrow \tanh \left(\frac{g_i}{\sqrt{\hat{v}_i} + \epsilon} \right) \quad (13)$$

Yet another desired property highlighted in Figure 4 is that near the jump, the ratio of the gradient magnitudes to either side of the jump is to be preserved between the original and normed gradient cases. This is important for the convergence dynamics of the system discussed in Section 4.3. In dynamic situations, the gradient normalization solution (12) approximates this feature as well.

Figure 5 shows training curves on the toy L_2 quantization error problem across various bit-widths, input scales, and optimization algorithms. Raw gradient with SGD fails for large σ and converges too slowly for small σ , as we would expect from Sections 4.1 and 4.2. Additionally, they have b, σ -dependent stability once converged. Switching from raw to log threshold gradients, we see that log gradient with Adam performs well, yet log gradient with SGD performs poorly, with weak convergence rates for small σ and divergence for large σ . However, after performing gradient normalization (13), normed log gradient with SGD performs well, demonstrating that lack of proper gradient norming is the main issue preventing convergence using standard gradient descent. Besides the differing convergence rates, another characteristic becomes immediately obvious - stability after convergence. For example, raw gradient method tends to oscillate wildly between multiple integer-level log thresholds, whereas normed log gradient

method is better behaved and tends to stay within a single integer log threshold band.

Adam optimizer: While gradient norming (13) led to good results with SGD, we note that Adam without this gradient norming also works quite well. It is easy to see why this is - Adam has built-in gradient norming [20]. Thus we can avoid redefining the gradients by simply using an optimizer that includes adaptive gradients, such as Adam or RMSprop [13]. While RMSprop appears to superficially resemble (13) more closely than Adam, we suspect Adam has better behavior in the absence of gradient clipping due to its use of moments to smooth the gradients. To use Adam safely, we derive rough bounds on the learning rate and momentum parameters to ensure the oscillations seen in Figure 5 for log gradient with Adam do not exceed a single integer bin. This is important because if they move across bins often, the network may have more trouble adapting to the changing distributions from a given quantized layer, in an effect that may be similar to the motivation for batch normalization [15].

4.3. Convergence

One primary cause of the sharp gradient jumps seen in Figure 4 is our insistence on power-of-2 scaling. In the forward pass, features downstream from the quantized layer are completely unaware of intermediate non-power-of-2 scale-factors so there are sharp jumps at integral $\log_2 t$, similar to what might be observed when using the STE for traditional quantization. The net effect is a bang-bang like operation.

In more detail, for a given input distribution there is some critical integer threshold $\log_2 t^*$ before which the gradients are negative (causing positive threshold updates) and after which the gradients are positive. This negative feedback will force the threshold to oscillate around $\log_2 t^*$. The gradients g_l and g_h on either side of $\log_2 t^*$ tend to be fairly constant within a distance 1 of $\log_2 t^*$ due to power-of-2 scaling. For simplicity, assume $|g_l| > |g_h|$ so that the ratio $r_g = -g_l/g_h > 1$. As r_g grows, we would expect the following behavior: the threshold stays in the higher bin for a while, slowly decaying until reaching the lower bin, at which point a large $|g_l|$ causes it to jump back to the higher bin, where it begins a slow decay again. This behavior can be observed in the left plots of Figure 5 and are shown in more detail in Figure 9.

If normed log gradients and SGD are used together, the dynamics are fairly simple. Let $\log_2 t_i \leftarrow \log_2 t_{i-1} - \alpha \tilde{g}_i$ be the SGD update on normed log gradient \tilde{g}_i (13). Then because $|\tilde{g}_i| \leq 1$ by design, a given jump in the sawtooth-like pattern will have magnitude bounded by learning rate α . Thus by selecting $\alpha \ll 1$, we can ensure convergence within a threshold bin.

However in our experiments, we used the implementa-

tionally simpler approach of unnormed log gradients with the Adam optimizer. While simpler to implement, the analysis is more complicated due to the second-order nature of the optimizer. Adam has three key hyperparameters: α, β_1, β_2 and operates by keeping track of a moving mean of gradients $m_i \leftarrow \beta_1 m_{i-1} + (1 - \beta_1)g_i$ and a moving variance $v_i \leftarrow \beta_1 v_{i-1} + (1 - \beta_1)g_i^2$ before applying update rule $\theta_i \leftarrow \theta_{i-1} - \alpha \cdot m_i / \sqrt{v_i}$. In practice, bias correction is used to get \hat{m}_i, \hat{v}_i , but when considering settling dynamics for $i \rightarrow \infty$, this bias correction is insignificant. Typical values are $\alpha \approx 10^{-3}, \beta_1 \approx 0.9, \beta_2 \approx 0.999$.

In Appendix B, a detailed analysis of convergence for Adam is carried out. From this analysis a simple set of guidelines emerge. First, the learning rate is set to guarantee $\alpha < 0.1/\sqrt{p}$. Next, we ensure $1/e < \beta_1 < 1$ to satisfy the limits of our analysis. Finally, we make sure $r_g \approx p \ll 1/(1 - \beta_2) \Rightarrow 1 - \beta_2 \ll 1/p$. These results are summarized in Table 1. For simplicity, we use $\alpha = 0.01, \beta_1 = 0.9, \beta_2 = 0.999$ for all of our training.

| Bit-width | b | 4 | 8 |
|-----------|--|---------------|----------------|
| α | $\leq \frac{0.1}{\sqrt{2^{b-1}-1}}$ | ≤ 0.035 | ≤ 0.009 |
| β_1 | $\geq 1/e$ | $\geq 1/e$ | $\geq 1/e$ |
| β_2 | $\geq 1 - \frac{0.1}{2^{b-1}-1}$ | ≥ 0.99 | ≥ 0.999 |
| Steps | $\approx \alpha^{-1} + (1 - \beta_2)^{-1}$ | ≈ 100 | ≈ 1000 |

Table 1. Guidelines for log threshold training with Adam, assuming $b = 2^{b-1} - 1$ for signed data.

5. Framework for Trained Quantization

We released Graffitist⁶, an end-to-end software stack built on top of TensorFlow to quantize and retrain deep neural networks using our ALT method. It is in experimental stages as we continue to add support for more operation types, layer topologies, network styles, graph optimizations, and compression techniques. Graffitist stands on the shoulders of giants and the interface is inspired in part by earlier tools from TensorFlow [36, 37].

5.1. Graph Optimizations

Graffitist applies several optimizations to the input graph prior to quantization. For example, folding batch normalization layers into preceding convolutional or fully connected or depthwise convolutional layers' weights. We adopt the following best practices from [18, 21, 37]: (a) ensure folded batch norms in training and inference graphs are mathematically equivalent (i.e., distributions seen during training match those during inference); (b) apply batch

⁶Code available at <https://github.com/Xilinx/graffitist>.

norm corrections for switching between batch and moving average statistics to reduce jitter in training folded weights due to noisy batch updates; (c) freeze batch norm moving mean and variance updates post convergence for improved accuracy. Other optimizations include collapsing concat-of-concat layers into single concat, splicing identity nodes not involved in control edges, transforming average pool layers into depthwise conv layers with reciprocal⁷ multiplier as weights, and explicitly merging input scales for scale preserving ops such as concat, bias-add, eltwise-add, and maximum (for leaky relu).

5.2. Quantization Modes

Graffitist allows for quantization in either static mode or retrain mode.

Static Mode. Quantization thresholds (hence scale factors) are determined based on statistics of weights and activations derived from a calibration dataset. Specifically, weight thresholds (per-tensor) are set to the maximum absolute value, and activation thresholds (per-tensor) are chosen such as to minimize the symmetric Kullback-Leibler-J distance [8] for each quantization layer locally. This is done in a strictly topological order to ensure inputs to a layer are quantized (and fixed) prior to quantizing the current layer. The entire optimization and calibration process is automated and only requires a single API call to Graffitist.

Retrain Mode. Quantization thresholds and weights are simultaneously trained on a global loss using our ALT method. Recovery is achieved within 5 epochs of retraining. This requires two separate API calls to Graffitist - first to generate a quantized training graph which can be trained using native TensorFlow, and second to generate the equivalent quantized inference graph which uses weights and thresholds from the previously trained checkpoint.

5.3. Layer Precisions

While Graffitist supports configurable bit-widths for weights and activations, for the scope of this paper we use two modes; INT8: 8/8 (W/A) and INT4: 4/8 (W/A). In the absence of a 4x8 multiplier, the INT4 mode still allows for 50% weight compression (double packing weights per byte) and reduced memory bandwidth cost for fetching weights. The internal precisions for different layer topologies are defined below. Quantization layers marked as q' indicate that their scale-factors are explicitly merged / shared. To avoid double quantization, input tensors are assumed to be already quantized by the previous layer, with the exception of the primary input (placeholder) which is explicitly quantized.

- Compute layers (e.g., conv, matmul, depthwise conv) are quantized as:

$$q_8 \left(q'_{16} \left(\sum (q_{8/4}(w) \cdot q_8(x)) \right) + q'_{16}(b) \right),$$

⁷Reciprocal being $1/F^2$ where F is the kernel size.

where x is the input tensor, w is the weight tensor, and b is the bias tensor. If followed by a ReLU or ReLU6 activation function, the last $q_8()$ stage is delayed to until after ReLU/ReLU6, and uses unsigned datatype to utilize the extra sign bit.

- Eltwise-add layer is quantized as:

$$q_8 (q'_8(x) + q'_8(y)),$$

where x and y are the input tensors. Similar to the compute layer case, the last $q_8()$ stage is delayed and uses unsigned datatype if followed by ReLU/ReLU6.

- Leaky ReLU is quantized as:

$$q_8 (\max (q'_{16}(x), q'_{16} (q_{16}(\alpha) \cdot q'_{16}(x)))),$$

where x is the input tensor, and α is the slope of activation function for negative inputs. The last $q_8()$ stage on the previous compute layer is skipped when it is followed by Leaky ReLU. Instead a $q_{16}()$ stage is used to retain high internal precision for the α -multiply op.

- Average pool is quantized as:

$$q_8 \left(\sum (q_{18}(r) \cdot q_8(x)) \right),$$

where x is the input tensor, and r is the reciprocal.

- Concat is not quantized because the input scales are merged explicitly, and hence it is lossless:

$$\text{concat}(q'_8(x), q'_8(y), q'_8(z)),$$

where x , y , and z are input tensors.

5.4. Fused Kernel Implementation

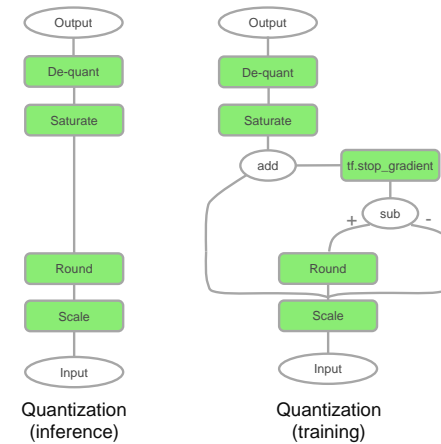


Figure 6. Quantization layer using the STE. During backpropagation, the round function is hidden using `tf.stop_gradient`.

The quantization layer defined in (4) and (6) may be trivially implemented using native TensorFlow ops and

`tf.stop_gradient` as depicted in Figure 6. However this low-level implementation has a large memory footprint during training due to the need for storing intermediate tensors for gradient computation in the backward pass. This impacts the maximum batch size that can fit on a single GPU. To resolve this, Graffitist comes packaged with fused quantization kernels that are pre-compiled for CPU/GPU. The fused implementation is efficient, helps avoid memory overhead and allows training using larger batch sizes compared to the native implementation.

6. Experiments

We evaluate ALT on variants of five classes of CNNs trained and validated on ImageNet (ILSVRC14) classification dataset [28]. The networks include VGG {16, 19} [30], Inception v{1, 2, 3, 4} [32, 15, 33, 31], ResNet v1 {50, 101, 152} [12], MobileNet v{1, 2} 1.0 224 [14, 29], and DarkNet 19 [27]. We obtained the models, pre-trained weights (FP32) and pre-processing for each of these networks from the TF-Slim model zoo [38] except for DarkNet 19 which was converted to TensorFlow using DW2TF [11]. Calibration sets are prepared for each network using a batch of 50 unlabeled images, randomly sampled from the validation set, with applied pre-processing. This is used for initializing the thresholds in both static and retrain modes.

6.1. Comparisons

We are interested in a scalable, hardware-friendly and production-ready approach to INT8/INT4 quantization that maps well on generic fixed-point hardware. While our simplifying constraints (from Section 3.1) may not be ideal for lower bit-widths, the fundamentals of ALT are more generally applicable by simply removing these constraints. To limit the scope of this paper to the least-common-denominator fixed-point quantization, we do not make comparisons with other state-of-the-art low-bitwidth quantization schemes. Instead we draw comparisons of ALT (wt+th) retraining to static quantization and wt-only retraining. We can derive many interesting insights from this analysis.

6.2. Threshold Initializations and Freezing

When thresholds are not trained, they are initialized to MAX for weights, and KL-J distance calibrated for activations. However when training thresholds, we find it useful to initialize the weight thresholds based on n standard deviations or percentile of the weight distribution rather than MAX. Table 2 summarizes the threshold initialization scheme we used in all our experiments.

In Section 4.3, we discussed the post-convergence oscillations of thresholds around the critical integer threshold $\log_2 t^*$ due to our power-of-2 scaling constraint. When thresholds cross this integer level, it can change the distributions of downstream activations, requiring weights and

| Mode | Threshold Initialization | |
|---------|--------------------------|--------------------|
| | weights | activations |
| Static | MAX | KL-J |
| Retrain | wt wt,th | MAX 3SD KL-J |

Table 2. Threshold initialization scheme using MAX or 3SD initialization for weights and KL-J distance calibrated for activations.

thresholds of the following layers to adapt to it. To minimize this effect, we incrementally freeze thresholds starting at $1000 \cdot (24/N)$ steps, once every 50 steps in the order of increasing absolute gradient magnitude, if they are on the correct side of $\log_2 t^*$ (determined using an EMA).

6.3. Implementation Details

Before exporting the models to TensorFlow protocol buffers (.pb) for Graffitist to absorb, we make the following synthetic modifications: (i) replace `tf.reduce_mean` with `tf.nn.avg_pool` (if any), (ii) remove auxiliary logit layers (if any), and (iii) remove dropouts (if any). Additionally, we disable data-augmentation (e.g., random flip / crop) during retraining. These modifications are done keeping in mind that ALT training focuses primarily on learning thresholds through backpropagation, while allowing previously trained weights to be fine-tuned using a relatively small learning rate. As expected, most of the recovery is achieved within a fraction of an epoch due to thresholds converging, and the rest of it (up to 5 epochs) is just weights adjusting to the new thresholds. Because the overall training steps required with ALT are so few compared to from-scratch training, and that pre-trained weight distributions are not allowed to wildly change (overfit), we find it best to disable data-augmentation and dropout regularization.

Based on the analysis in Sections 4.2 and 4.3, we use the Adam optimizer with parameters $\beta_1 = 0.9$ and $\beta_2 = 0.999$ for training thresholds and weights. The initial learning rate is set to $1e-2$ for thresholds and $1e-6$ for weights. Learning rates are decayed exponentially (with staircase enabled) by a factor of 0.94 every $3000 \cdot (24/N)$ steps for weights and by a factor of 0.5 every $1000 \cdot (24/N)$ steps for thresholds, where N is the batch size. We use a batch size of 24 for all networks except for ResNet v1 152 and Inception v4 for which a batch of 16 is used. Softmax cross-entropy loss is used to compute quantization threshold gradients and this loss, together with weight regularization (if any), are used to compute weight gradients. Batch norm moving means and variances are frozen after 1 epoch.

6.4. Results

Table 3 reports the single-crop ImageNet validation accuracy for 12 networks. Default image sizes are used - 299×299 for Inception v{3, 4}, 256×256 for Darknet

| Mode | Precision | Bit-width | Accuracy (%) | Epochs |
|-----------------------------|-----------|-----------|--------------|--------|
| | (W/A) | top-1 | top-5 | |
| VGG 16 | | | | |
| | FP32 | 32/32 | 70.9 | 89.8 |
| Static | INT8 | 8/8 | 70.4 | 89.7 |
| Retrain | wt | FP32 | 32/32 | 71.9 |
| | wt | INT8 | 8/8 | 71.8 |
| | wt,th | INT8 | 8/8 | 71.7 |
| | wt,th | INT4 | 4/8 | 71.5 |
| VGG 19 | | | | |
| | FP32 | 32/32 | 71.0 | 89.8 |
| Static | INT8 | 8/8 | 70.4 | 89.7 |
| Retrain | wt | FP32 | 32/32 | 71.8 |
| | wt | INT8 | 8/8 | 71.7 |
| | wt,th | INT8 | 8/8 | 71.7 |
| | wt,th | INT4 | 4/8 | 71.2 |
| Inception v1 | | | | |
| | FP32 | 32/32 | 69.8 | 89.6 |
| Static | INT8 | 8/8 | 68.6 | 88.9 |
| Retrain | wt | FP32 | 32/32 | 70.3 |
| | wt | INT8 | 8/8 | 70.6 |
| | wt,th | INT8 | 8/8 | 70.7 |
| | wt,th | INT4 | 4/8 | 67.2 |
| Inception v2 | | | | |
| | FP32 | 32/32 | 74.0 | 91.8 |
| Static | INT8 | 8/8 | 73.1 | 91.3 |
| Retrain | wt | FP32 | 32/32 | 74.3 |
| | wt | INT8 | 8/8 | 74.4 |
| | wt,th | INT8 | 8/8 | 74.4 |
| | wt,th | INT4 | 4/8 | 71.9 |
| Inception v3 | | | | |
| | FP32 | 32/32 | 78.0 | 93.9 |
| Static | INT8 | 8/8 | 76.8 | 93.3 |
| Retrain | wt | FP32 | 32/32 | 78.3 |
| | wt | INT8 | 8/8 | 78.2 |
| | wt,th | INT8 | 8/8 | 78.3 |
| | wt,th | INT4 | 4/8 | 76.4 |
| Inception v4 | | | | |
| | FP32 | 32/32 | 80.2 | 95.2 |
| Static | INT8 | 8/8 | 79.4 | 94.6 |
| Retrain | wt | FP32 | 32/32 | 80.2 |
| | wt | INT8 | 8/8 | 80.1 |
| | wt,th | INT8 | 8/8 | 80.1 |
| | wt,th | INT4 | 4/8 | 78.9 |
| MobileNet v1 1.0 224 | | | | |
| | FP32 | 32/32 | 71.0 | 90.0 |
| Static | INT8 | 8/8 | 0.6 | 3.6 |
| Retrain | wt | FP32 | 32/32 | 71.1 |
| | wt | INT8 | 8/8 | 67.0 |
| | wt,th | INT8 | 8/8 | 71.1 |
| | wt,th | INT4 | 4/8 | — |
| MobileNet v2 1.0 224 | | | | |
| | FP32 | 32/32 | 70.1 | 89.5 |
| Static | INT8 | 8/8 | 0.3 | 1.2 |
| Retrain | wt | FP32 | 32/32 | 71.7 |
| | wt | INT8 | 8/8 | 68.2 |
| | wt,th | INT8 | 8/8 | 71.8 |
| | wt,th | INT4 | 4/8 | — |
| DarkNet 19 | | | | |
| | FP32 | 32/32 | 73.0 | 91.4 |
| Static | INT8 | 8/8 | 68.7 | 89.7 |
| Retrain | wt | FP32 | 32/32 | 74.4 |
| | wt | INT8 | 8/8 | 72.9 |
| | wt,th | INT8 | 8/8 | 74.5 |
| | wt,th | INT4 | 4/8 | 73.2 |
| ResNet v1 50 | | | | |
| | FP32 | 32/32 | 75.2 | 92.2 |
| Static | INT8 | 8/8 | 74.3 | 91.7 |
| Retrain | wt | FP32 | 32/32 | 75.4 |
| | wt | INT8 | 8/8 | 75.3 |
| | wt,th | INT8 | 8/8 | 75.4 |
| | wt,th | INT4 | 4/8 | 74.4 |
| ResNet v1 101 | | | | |
| | FP32 | 32/32 | 76.4 | 92.9 |
| Static | INT8 | 8/8 | 74.8 | 92.0 |
| Retrain | wt | FP32 | 32/32 | 76.6 |
| | wt | INT8 | 8/8 | 76.3 |
| | wt,th | INT8 | 8/8 | 76.4 |
| | wt,th | INT4 | 4/8 | 75.7 |
| ResNet v1 152 | | | | |
| | FP32 | 32/32 | 76.8 | 93.2 |
| Static | INT8 | 8/8 | 76.2 | 93.0 |
| Retrain | wt | FP32 | 32/32 | 76.8 |
| | wt | INT8 | 8/8 | 76.7 |
| | wt,th | INT8 | 8/8 | 76.7 |
| | wt,th | INT4 | 4/8 | 76.0 |

Table 3. Quantization accuracy achieved on different ImageNet CNNs for static quantization, weight-only quantized retraining, and weight+threshold quantized retraining (ALT). Training is run until validation accuracy plateaus (max 5 epochs). We also compare to floating-point retraining to isolate the impact of our quantization methods from our training setup.

19 and 224 × 224 for all other networks. Standard pre-processing for each network is applied to center crop, resize, and normalize the input data.

The different trials include pre-trained FP32 baseline, static INT8 run, and 4 retrain runs - FP32 wt-only, INT8 wt-only, INT8 wt+th and INT4 wt+th. FP32 baseline numbers are reported as validated on our end. For an unbiased comparison, we train the FP32 weights using the same proce-

dure (optimizers, learning rates, decay, freeze etc.) as with our quantized retraining, except without the threshold training logic. This FP32 wt-only retraining only serves as a fair baseline to our INT8 and INT4 retrain results. That said, we do not use the retrained FP32 weights to initialize any of our INT8/INT4 retraining runs, and they always start from pre-trained FP32 weights. This is done to keep the overhead of retraining to a minimum.

7. Discussion

The validation accuracy and epoch count corresponding to the best checkpoint are noted in Table 3. As we see, all the networks converge within 5 epochs. Variance on the reported accuracy stems from a few sources (in decreasing order of impact): (a) best rather than mean validation (our findings in Section 7.3 suggest this variance is within 0.2%), (b) non-determinism due to inexact floating point math (empirically within 0.1%), (c) round to one decimal (bound to 0.05%). Keeping these variance bounds on accuracy in mind, we can draw interesting insights into the benefits of ALT training.

7.1. Insights from ALT Training

Our experiments demonstrate floating point accuracy for 8-bit quantization and near-floating-point accuracy for 4-bit quantization for most networks. We see that static quantization incurs a higher loss than retrained methods. This is expected because (a) weights are not trained to adapt to the quantized network, and (b) quantization thresholds are picked using local statistics instead of being optimized on a global loss. For networks that are easier to quantize to INT8 (e.g., VGGs, Inceptions, ResNets), we find that retraining weights alone while fixing thresholds to their pre-calibrated values (based on Table 2) is sufficient. In such cases, ALT (wt+th) retraining shows no added benefit. However, for networks known to be difficult to quantize (e.g., MobileNets, DarkNets), ALT (wt+th) retraining yields up to 4% higher top-1 accuracy compared to wt-only training for INT8, and can match FP32 accuracy even with per-tensor, uniform symmetric, power-of-2 scaling constraints. This demonstrates the range-precision tradeoff through trained thresholds in action. For lower precisions such as INT4, we find that wt-only training does not recover, and so ALT (wt+th) retraining is necessary. The INT4 accuracy falls short of FP32, and we believe this maybe due to (a) our quantization constraints in Section 3.1, and (b) the first/last layers not retaining full precision⁸.

7.2. MobileNet Comparisons

For more difficult networks such as MobileNets, it is well known that symmetric, per-tensor quantization post-training or through calibrate-only methods is detrimental [21, 10]. We believe this is true, in particular due to the use of depthwise convolutions with irregular weight distributions and widely varying ranges between channels. With wt-only retraining we are only able to recover to within 4% of floating-point accuracy. However, with ALT (wt+th) retraining, our results for 8-bit are the highest we have seen using symmetric, power-of-2 scaled, per-tensor quantiza-

⁸We quantize first/last layers to a minimum of INT8, so that they can be mapped on the same fixed-point hardware used for other layers.

| Method | Precision | Quantization Scheme | top-1 |
|-----------------------------|-----------|---------------------------------------|-------|
| MobileNet v1 1.0 224 | | | |
| | FP32 | | 70.9 |
| Google | INT8 | per-channel, symmetric, real scaling | 70.7 |
| | INT8 | per-tensor, asymmetric, real scaling | 70.0 |
| | FP32 | | 71.1 |
| Ours | INT8 | per-tensor, symmetric, p-of-2 scaling | 71.1 |
| MobileNet v2 1.0 224 | | | |
| | FP32 | | 71.9 |
| Google | INT8 | per-channel, symmetric, real scaling | 71.1 |
| | INT8 | per-tensor, asymmetric, real scaling | 70.9 |
| | FP32 | | 71.7 |
| Ours | INT8 | per-tensor, symmetric, p-of-2 scaling | 71.8 |

Table 4. Comparison of MobileNet quantization accuracy between Google’s (from Table 4 of [21]) and ours. Our constraints are strictly more difficult than either of their constraints, yet achieve much higher accuracy.

tion, even matching floating-point accuracy with no loss. In Table 4 we draw a few comparisons with Google’s quantization-aware training results for MobileNets. As seen, we incur no loss with INT8 quantization even with stricter constraints. We believe this is due to the fact that our threshold gradient formulation is in fact able to balance range-precision effectively.

In Figure 7 we analyze the retrained distributions for a few quantized layers in MobileNet v1, highlighting the importance of range-precision trade-off. As seen with the depthwise separable layers’ weights, the trained thresholds move-in from their initialized values by up to 3 integer bins in the log domain, favoring precision over dynamic range. For some other layers, the thresholds move-out from their initialized values, favoring range over precision.

Figure 8 shows a histogram of trained threshold deviations for different networks under 8-bit and 4-bit quantized retraining. We find that larger positive deviations are seen in the 8-bit case compared to the 4-bit case. This intuitively makes sense as the method decides to favor range with more bits of precision, but cuts back on range when only few bits of precision are available.

7.3. Best or Mean Validation

We run validation every 1000 training steps and save the best top-1 score checkpoint. This approach was initially driven by a desire to better understand convergence and stability properties with our method, but we continued using it since intermediate validation was not too expensive for 5 epochs of retraining. However a valid concern is that this intermediate validation introduces a positive bias to our results through cherry-picking. We compare this positive-biased validation method to simply taking the average of validation scores at fixed intervals: 20%, 40%, 60%, 80% and 100% of the fifth epoch. As noted in Table 5, the differences between these methods on the top-1 accuracy are

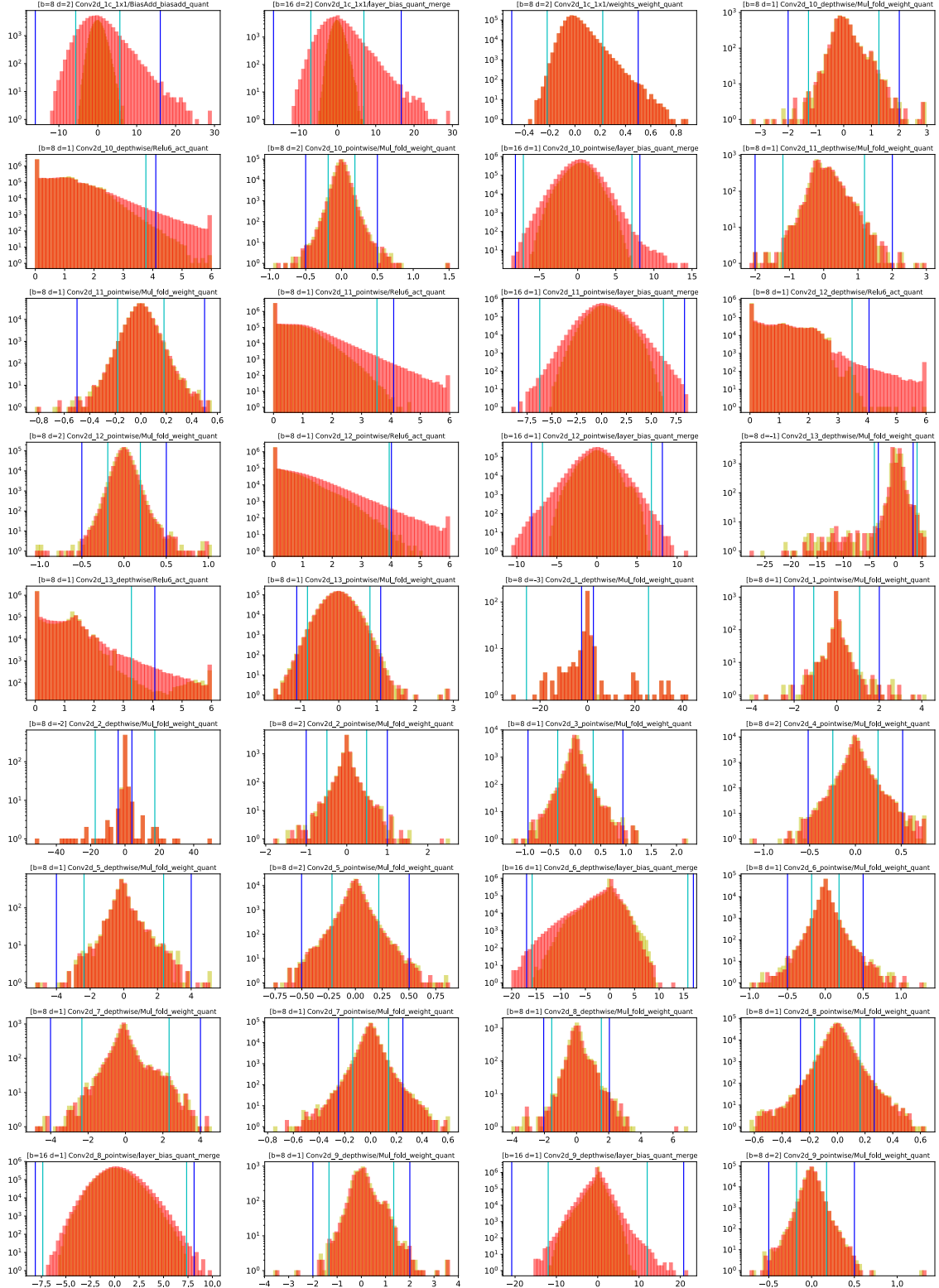


Figure 7. Weight and activation distributions of MobileNet v1 before (yellow) and after (red) quantized ALT (wt+th) retraining for thresholds that changed by non-zero integer amount in log-domain. Initial thresholds (cyan) and trained thresholds (blue) are also plotted. Also indicated are bit-width b and threshold deviation $d := \Delta \lceil \log_2 t \rceil$ for the quantized layer. We note that depthwise-separable convolutions have unique threshold training behavior with a strong preference for precision compared to range.

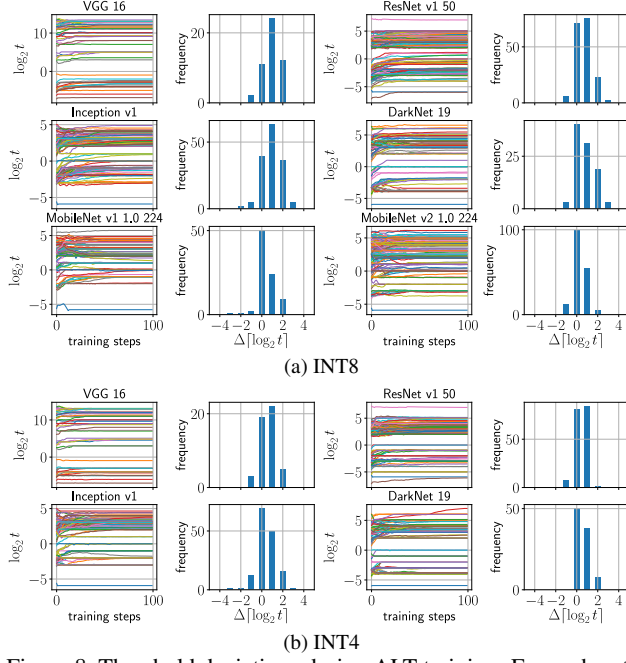


Figure 8. Threshold deviations during ALT training. For each network, the left plot shows the value of each of the thresholds over the first 100 training steps, and the right plot shows a histogram of deviations from the start (initialized thresholds) to the end (trained thresholds) of training.

0.1% and 0.2% for MobileNet v1 and VGG 16 respectively, suggesting that cherry-picking only results in a minor positive bias on our reported accuracy.

| | Accuracy (%) | | Epochs |
|-----------------------------|--------------|-------------|--------|
| | top-1 | top-5 | |
| MobileNet v1 1.0 224 | | | |
| 70.982 | 89.886 | 4.2 | |
| 70.986 | 89.860 | 4.4 | |
| 71.076 | 89.930 | 4.6 | |
| 71.000 | 89.870 | 4.8 | |
| 71.022 | 89.944 | 5.0 | |
| Mean | 71.0 | 89.9 | |
| Best | 71.1 | 90.0 | 2.1 |
| VGG 16 | | | |
| 71.448 | 90.438 | 4.2 | |
| 71.462 | 90.456 | 4.4 | |
| 71.434 | 90.436 | 4.6 | |
| 71.500 | 90.426 | 4.8 | |
| 71.458 | 90.456 | 5.0 | |
| Mean | 71.5 | 90.4 | |
| Best | 71.7 | 90.4 | 0.9 |

Table 5. Best validation (cherry-picked) is compared to the average of five validations (at pre-determined steps) in the last epoch, for two networks.

8. Conclusion

In Section 3, we presented a quantization threshold training scheme amenable to most generic fixed-point hardware by constraining our method to uniform, symmetric, power-of-2 scaled, per-tensor quantization. We showed that our quantizer’s gradient formulation allowed a unique range-precision trade-off, essential for high accuracy quantized networks. We demonstrated that training was possible despite all of our constraints by utilizing log-domain threshold training and adaptive gradient optimization. In Section 4, we provided analytical arguments for the general robustness of our adaptive-gradient log-domain threshold (ALT) training technique. In Section 5, we presented a framework called Graffitist for automatically quantizing TensorFlow graphs with our methods. In Section 6, we empirically validated our methods on a suite of common ImageNet CNNs. Finally, in Sections 7, we provided insightful discussions on ALT training and state-of-the-art results for 8-bit MobileNet quantization.

Our work and results demonstrate the effectiveness of our techniques for high accuracy quantization of neural networks on fixed-point hardware. While our work covers a major use case for quantization, there are many other quantization flavors we could explore in future work. For example, it would be useful to see how well the techniques we designed for strict power-of-2 scaling generalize to non power-of-2 scale-factors. Some additional relaxations of our constraints we could explore include per-channel rather than per-tensor quantization, which could potentially allow for more aggressive bitwidths on difficult networks like MobileNets, and non-symmetric or even non-uniform quantization schemes, where threshold training via backpropagation and gradient descent has been tried with mild success. We would not be surprised to see our methods and analysis techniques have broader applicability for more general classes of quantizers.

9. Acknowledgements

We thank Engin Tunali, Ramon Uribe, Sean Settle, Paolo D’Alberto, Armin Banaei, Ephrem Wu, Nicholas Fraser, Ralph Wittig from Xilinx, and Elaina Chai, Boris Murmann from Stanford for valuable discussions and comments.

References

- [1] M. Abadi, A. Agarwal, P. Barham, E. Brevdo, Z. Chen, C. Citro, G. S. Corrado, A. Davis, J. Dean, M. Devin, et al. Tensorflow: Large-scale machine learning on heterogeneous distributed systems. *arXiv preprint arXiv:1603.04467*, 2016.
- [2] M. Abadi, P. Barham, J. Chen, Z. Chen, A. Davis, J. Dean, M. Devin, S. Ghemawat, G. Irving, M. Isard, et al. Tensorflow: A system for large-scale machine learning. *arXiv preprint arXiv:1605.08695*, 2016.

[3] C. Baskin, N. Liss, Y. Chai, E. Zheltonozhskii, E. Schwartz, R. Giryes, A. Mendelson, and A. M. Bronstein. Nice: Noise injection and clamping estimation for neural network quantization. *arXiv preprint arXiv:1810.00162*, 2018.

[4] Y. Bengio, N. Léonard, and A. Courville. Estimating or propagating gradients through stochastic neurons for conditional computation. *arXiv preprint arXiv:1308.3432*, 2013.

[5] Z. Cai, X. He, J. Sun, and N. Vasconcelos. Deep learning with low precision by half-wave gaussian quantization. *arXiv preprint arXiv:1702.00953*, 2017.

[6] J. Choi, Z. Wang, S. Venkataramani, P. I.-J. Chuang, V. Srinivasan, and K. Gopalakrishnan. Pact: Parameterized clipping activation for quantized neural networks. *arXiv preprint arXiv:1805.06085*, 2018.

[7] M. Courbariaux, I. Hubara, D. Soudry, R. El-Yaniv, and Y. Bengio. Binarized neural networks: Training deep neural networks with weights and activations constrained to + 1 or -1. *arXiv preprint arXiv:1602.02830*, 2016.

[8] P. D’Alberto and A. Dasdan. Non-parametric information-theoretic measures of one-dimensional distribution functions from continuous time series. In *Proceedings of the 2009 SIAM International Conference on Data Mining*, pages 685–696. SIAM, 2009.

[9] S. K. Esser, J. L. McKinstry, D. Bablani, R. Appuswamy, and D. S. Modha. Learned step size quantization. *arXiv preprint arXiv:1902.08153*, 2019.

[10] A. Goncharenko, A. Denisov, S. Alyamkin, and E. Terentev. Fast adjustable threshold for uniform neural network quantization. *arXiv preprint arXiv:1812.07872*, 2018.

[11] Y. Hao and S. R. Jain. Darknet to tensorflow (DW2TF). <https://github.com/jinyu121/DW2TF/releases/tag/v1.1>, 2018.

[12] K. He, X. Zhang, S. Ren, and J. Sun. Deep residual learning for image recognition. *arXiv preprint arXiv:1512.03385*, 2015.

[13] G. Hinton, N. Srivastava, and K. Swersky. Lecture 6a overview of mini-batch gradient descent (2012). *Coursera Lecture slides* <https://class.coursera.org/neuralnets-2012-001/lecture>, 2012.

[14] A. G. Howard, M. Zhu, B. Chen, D. Kalenichenko, W. Wang, T. Weyand, M. Andreetto, and H. Adam. Mobilenets: Efficient convolutional neural networks for mobile vision applications. *arXiv preprint arXiv:1704.04861*, 2017.

[15] S. Ioffe and C. Szegedy. Batch normalization: Accelerating deep network training by reducing internal covariate shift. *arXiv preprint arXiv:1502.03167*, 2015.

[16] B. Jacob et al. Gemmlowp: Building a quantization paradigm from first principles. <https://github.com/google/gemmlowp/blob/master/doc/quantization.md#domain-specific-constraint-the-real-value-0-must-be-exactly-representable>, 2016.

[17] B. Jacob et al. Gemmlowp: Efficient handling of offsets. <https://github.com/google/gemmlowp/blob/master/doc/low-precision.md#efficient-handling-of-offsets>, 2016.

[18] B. Jacob, S. Kligys, B. Chen, M. Zhu, M. Tang, A. Howard, H. Adam, and D. Kalenichenko. Quantization and training of neural networks for efficient integer-arithmetic-only inference. *arXiv preprint arXiv:1712.05877*, 2017.

[19] S. Jung, C. Son, S. Lee, J. Son, Y. Kwak, J.-J. Han, S. J. Hwang, and C. Choi. Learning to quantize deep networks by optimizing quantization intervals with task loss. *arXiv preprint arXiv:1808.05779*, 2018.

[20] D. P. Kingma and J. Ba. Adam: A method for stochastic optimization. *arXiv preprint arXiv:1412.6980*, 2014.

[21] R. Krishnamoorthi. Quantizing deep convolutional networks for efficient inference: A whitepaper. *arXiv preprint arXiv:1806.08342*, 2018.

[22] F. Li, B. Zhang, and B. Liu. Ternary weight networks. *arXiv preprint arXiv:1605.04711*, 2016.

[23] J. L. McKinstry, S. K. Esser, R. Appuswamy, D. Bablani, J. V. Arthur, I. B. Yildiz, and D. S. Modha. Discovering low-precision networks close to full-precision networks for efficient embedded inference. *arXiv preprint arXiv:1809.04191*, 2018.

[24] S. Migacz. 8-bit inference with tensorrt. In *GPU Technology Conference*, 2017.

[25] A. Mishra, E. Nurvitadhi, J. J. Cook, and D. Marr. Wrpn: wide reduced-precision networks. *arXiv preprint arXiv:1709.01134*, 2017.

[26] M. Rastegari, V. Ordonez, J. Redmon, and A. Farhadi. Xnor-net: Imagenet classification using binary convolutional neural networks. *arXiv preprint arXiv:1603.05279*, 2016.

[27] J. Redmon and A. Farhadi. Yolo9000: Better, faster, stronger. *arXiv preprint arXiv:1612.08242*, 2016.

[28] O. Russakovsky, J. Deng, H. Su, J. Krause, S. Satheesh, S. Ma, Z. Huang, A. Karpathy, A. Khosla, M. Bernstein, A. C. Berg, and L. Fei-Fei. ImageNet Large Scale Visual Recognition Challenge. *International Journal of Computer Vision (IJCV)*, 115(3):211–252, 2015.

[29] M. Sandler, A. Howard, M. Zhu, A. Zhmoginov, and L.-C. Chen. Mobilenetv2: Inverted residuals and linear bottlenecks. *arXiv preprint arXiv:1801.04381*, 2018.

[30] K. Simonyan and A. Zisserman. Very deep convolutional networks for large-scale image recognition. *arXiv preprint arXiv:1409.1556*, 2014.

[31] C. Szegedy, S. Ioffe, V. Vanhoucke, and A. Alemi. Inception-v4, inception-resnet and the impact of residual connections on learning. *arXiv preprint arXiv:1602.07261*, 2016.

[32] C. Szegedy, W. Liu, Y. Jia, P. Sermanet, S. Reed, D. Anguelov, D. Erhan, V. Vanhoucke, and A. Rabinovich. Going deeper with convolutions. *arXiv preprint arXiv:1409.4842*, 2014.

[33] C. Szegedy, V. Vanhoucke, S. Ioffe, J. Shlens, and Z. Wojna. Rethinking the inception architecture for computer vision. *arXiv preprint arXiv:1512.00567*, 2015.

[34] TensorFlow. FakeQuant API. https://www.tensorflow.org/versions/r1.13/api_docs/python/tf/quantization/fake_quant_with_min_max_vars, 2016.

[35] TensorFlow. FakeQuant threshold gradients. <https://github.com/tensorflow/tensorflow/>

blob/v1.13.1/tensorflow/core/kernels/fake_quant_ops_functor.h#L179-L187, 2016.

[36] TensorFlow. Graph transform tool. https://github.com/tensorflow/tensorflow/blob/v1.13.1/tensorflow/tools/graph_transforms/README.md, 2016.

[37] TensorFlow. Quantization-aware training. <https://github.com/tensorflow/tensorflow/blob/v1.13.1/tensorflow/contrib/quantize/README.md>, 2017.

[38] TensorFlow. Tf-slim pre-trained models. <https://github.com/tensorflow/models/blob/v1.13.0/research/slim/README.md#pre-trained-models>, 2017.

[39] D. Zhang, J. Yang, D. Ye, and G. Hua. Lq-nets: Learned quantization for highly accurate and compact deep neural networks. *arXiv preprint arXiv:1807.10029*, 2018.

[40] S. Zhou, Y. Wu, Z. Ni, X. Zhou, H. Wen, and Y. Zou. Dorefa-net: Training low bitwidth convolutional neural networks with low bitwidth gradients. *arXiv preprint arXiv:1606.06160*, 2016.

[41] C. Zhu, S. Han, H. Mao, and W. J. Dally. Trained ternary quantization. *arXiv preprint arXiv:1612.01064*, 2016.

A. Appendix: Cost of Affine Quantizer

A.1. Cross-terms due to zero-points

Consider⁹ two real numbers r_1 and r_2 and their product $r_3 = r_1 \cdot r_2$. Using the affine mapping from (2) to represent this, we get:

$$s_3(q_3 - z_3) = s_1(q_1 - z_1) \cdot s_2(q_2 - z_2), \quad (14)$$

which can be expressed as

$$q_3 = z_3 + \frac{s_1 s_2}{s_3} [q_1 q_2 - q_1 z_2 - q_2 z_1 + z_1 z_2]. \quad (15)$$

The cross-terms in (15) add complexity and often require special handling to remain efficient. While the added cost can be amortized over several accumulations of a matrix multiplication or convolution operation, it would still require optimizations¹⁰, both algorithmic and kernel-level.

By eliminating zero-points, the cross-terms vanish and the operation simplifies to:

$$q_3 = \frac{s_1 s_2}{s_3} [q_1 q_2]. \quad (16)$$

A.2. Real-valued scale-factors

With positive real scale-factors, the constant multiplier $s_1 s_2 / s_3$ in (16), which is empirically [18] found to be in the interval $(0, 1)$ can be expressed in the normalized form $2^{-n} s_0$ where n is a non-negative integer and s_0 is in the

⁹This example is adapted from Section 2.2 in [18].

¹⁰Some of which are covered in [17, 18, 21].

interval $[0.5, 1)$. In other words, the accumulator (storing $q_1 q_2$) needs to be scaled by a fixed-point multiplier that approximates s_0 and right-shifted by n bits (with round-to-nearest):

$$q_3 = 2^{-n} s_0 [q_1 q_2]. \quad (17)$$

However, by constraining scale-factors s_1, s_2, s_3 to strict power-of-2, the scaling operation reduces to a rather simple bit-shift (with round-to-nearest):

$$q_3 = 2^{-f} [q_1 q_2]. \quad (18)$$

B. Appendix: Analysis of Adam Convergence

Let T be the period of oscillations at convergence. If we assume $T \ll 1/(1 - \beta_2)$, then we can treat the moving variance estimate as if it is a constant $v_i = ((T - 1)g_h^2 + g_l^2)/T \approx g_l^2(1/r_g^2 + 1/T)$. However, we cannot make the same assumption for the relationship between T and β_1 . Instead, based on our earlier discussion in Section 4.3 of the bang-bang behavior, we assume that a gradient g_l is seen for a single step, then g_h is seen for $T - 1$ steps. Then for a given cycle of this behavior, $m_i = \beta_1^i(\beta_1 m_0 + (1 - \beta_1)g_l) + (1 - \beta_1^i)g_h$, where m_0 is the steady-state minimum mean during the cycle. Because this is steady-state, we can solve for m_0 and m_i :

$$m_i = \beta_1^i(\beta_1 m_0 + (1 - \beta_1)g_l) + (1 - \beta_1^i)g_h$$

$$m_T = m_0 = \beta_1^T(\beta_1 m_0 + (1 - \beta_1)g_l) + (1 - \beta_1^T)g_h$$

$$m_0 = \frac{\beta_1^T(1 - \beta_1) - (1 - \beta_1^T)/r_g}{1 - \beta_1^{T+1}} g_l \quad (19)$$

$$\frac{m_i}{g_l} = \beta_1^{i+1} \frac{\beta_1^T(1 - \beta_1) - (1 - \beta_1^T)/r_g}{1 - \beta_1^{T+1}}$$

$$+ \beta_1^i(1 - \beta_1 + \frac{1}{r_g}) - \frac{1}{r_g} \quad (20)$$

Adam updates look like $\theta_i \leftarrow \theta_{i-1} - \alpha \cdot m_i / \sqrt{v_i}$ or $\theta_i \leftarrow \theta_0 - \alpha \sum_{j=0}^i m_j / \sqrt{v_j}$. We can solve for T by finding when $\theta_T = \theta_0$ or $\sum_{i=0}^T m_i / \sqrt{v_i} = 0$. As an intermediate step, we find:

$$\Delta_t \theta = \sum_{i=0}^t \frac{m_i}{\sqrt{v_i}}$$

$$= \sum_{i=0}^t \frac{\beta_1^i \left(\beta_1 \frac{\beta_1^T(1 - \beta_1) - (1 - \beta_1^T)/r_g}{1 - \beta_1^{T+1}} + 1 - \beta_1 + \frac{1}{r_g} \right) - \frac{1}{r_g}}{\sqrt{1/r_g^2 + 1/T}}$$

$$= \frac{1}{\sqrt{\frac{1}{r_g^2} + \frac{1}{T}}} \left[\frac{1 - \beta_1^{t+1}}{1 - \beta_1} \left(\beta_1 \frac{\beta_1^T(1 - \beta_1) - (1 - \beta_1^T)/r_g}{1 - \beta_1^{T+1}} \right. \right.$$

$$\left. \left. + 1 - \beta_1 + \frac{1}{r_g} \right) - \frac{t+1}{r_g} \right] \quad (21)$$

Now, we set $\Delta_T \theta = 0$:

$$0 = \frac{1}{\sqrt{\frac{1}{r_g^2} + \frac{1}{T}}} \left[\frac{1 - \beta_1^{T+1}}{1 - \beta_1} \left(\beta_1 \frac{\beta_1^T (1 - \beta_1) - (1 - \beta_1^T) / r_g}{1 - \beta_1^{T+1}} \right. \right. \\ \left. \left. + 1 - \beta_1 + \frac{1}{r_g} \right) - \frac{T+1}{r_g} \right] \\ = \beta_1^{T+1} - \frac{\beta_1 (1 - \beta_1^T)}{r_g (1 - \beta_1)} + 1 - \beta_1^{T+1} + \frac{1 - \beta_1^{T+1}}{r_g (1 - \beta_1)} - \frac{T+1}{r_g} \\ T = r_g \quad (22)$$

The worst case happens when r_g is large, so if we substitute $T \leftarrow r_g$ and assume $r_g \gg 1$, we get:

$$\Delta_t \theta \approx \sqrt{r_g} \left[\frac{1 - \beta_1^{t+1}}{1 - \beta_1} \left(\beta_1 \frac{\beta_1^{r_g} (1 - \beta_1) - (1 - \beta_1^{r_g}) / r_g}{1 - \beta_1^{r_g+1}} \right. \right. \\ \left. \left. + 1 - \beta_1 + \frac{1}{r_g} \right) - \frac{t+1}{r_g} \right] \quad (23)$$

$$= \sqrt{r_g} \left[\frac{1 - \beta_1^{t+1}}{1 - \beta_1} c_1 - \frac{t+1}{r_g} \right] \quad (24)$$

where we replace the large expression in (23) with c_1 in (24). We now solve for the critical point of $\Delta_t \theta$ to determine $t_{max} = \text{argmax}_t \Delta_t \theta$.

$$0 = \frac{d}{dt} \Delta_t \theta \\ = \sqrt{r_g} \left[\frac{\ln(\beta_1^{-1}) \beta_1^{t_{max}+1}}{1 - \beta_1} c_1 - \frac{1}{r_g} \right] \\ \beta_1^{t_{max}+1} = \frac{1}{\ln(\beta_1^{-1})} \frac{1 - \beta_1}{r_g \cdot c_1} \quad (25) \\ = \frac{1}{\ln(\beta_1^{-1})} \frac{1 - \beta_1^{r_g+1}}{1 + r_g} \\ t_{max} = \log_{\beta_1} \left(\frac{1}{\ln(\beta_1^{-1})} \frac{1 - \beta_1^{r_g+1}}{1 + r_g} \right) - 1 \quad (26)$$

Plugging (25) and (26) into (24),

$$\Delta_{t_{max}} \theta \approx \sqrt{r_g} \left[\frac{c_1}{1 - \beta_1} - \frac{1}{r_g \ln(\beta_1^{-1})} \right. \\ \left. - \frac{1}{r_g} \log_{\beta_1} \left(\frac{1}{\ln(\beta_1^{-1})} \frac{1 - \beta_1^{r_g+1}}{1 + r_g} \right) \right] \quad (27)$$

To simplify this expression, note that $\beta_1 < 1$ and $r_g \gg 1$ so $1 - \beta_1^{r_g} \approx 1$. Then $c_1 / (1 - \beta_1) \approx 1 + 1/r_g \approx 1$ and:

$$\Delta_{t_{max}} \theta \approx \sqrt{r_g} \left[1 + \frac{1 + \ln(r_g \ln \beta_1^{-1})}{r_g \ln \beta_1} \right] \quad (28)$$

Further, if $1/e < \beta_1 < 1$, then the right term is negative and the expression has a simple upper bound:

$$\Delta_{t_{max}} \theta < \sqrt{r_g} \quad (29)$$

In practice, we notice that sometimes noise can cause θ to stay on the high-gradient side of the threshold boundary for multiple steps, causing the momentum to build up. Thus, to be safe, we recommend designing for $\Delta_{t_{max}} \theta < 10\sqrt{r_g}$.

A rough estimate for the number of steps needed for convergence is $\mathcal{O}(\Delta \lceil \log_2 t \rceil / (\alpha |\tilde{g}|))$. Because of adaptive gradients, $|\tilde{g}|$ should be close to 1, provided we allow enough time for historical variance to decay - $\mathcal{O}(1/(1 - \beta_2))$ steps¹¹. Thus, the overall number of steps would be $\mathcal{O}(\Delta \lceil \log_2 t \rceil / \alpha + \Delta \lceil \log_2 t \rceil / (1 - \beta_2))$. Assuming calibration is used, $\Delta \lceil \log_2 t \rceil$ should be close to 1, giving the simplified expression $\mathcal{O}(1/\alpha + 1/(1 - \beta_2))$ steps.

Finally, we address how to approximate r_g . The operation of crossing a threshold boundary moves some fraction f of inputs $\{x_i\}$ from the $n \leq \lfloor x/s \rfloor \leq p$ case to the $\lfloor x/s \rfloor < n$ or $\lfloor x/s \rfloor > p$ cases (assume only $\lfloor x/s \rfloor > p$ for simplicity from here on). Using the toy L_2 -loss model (9),

$$\nabla_{(\log_2 t)} L = s^2 \ln 2 \cdot \begin{cases} \left(\left\lfloor \frac{x}{s} \right\rfloor - \frac{x}{s} \right)^2 & \text{if } n \leq \left\lfloor \frac{x}{s} \right\rfloor \leq p, \\ n(n - x/s) & \text{if } \left\lfloor \frac{x}{s} \right\rfloor < n, \\ p(p - x/s) & \text{if } \left\lfloor \frac{x}{s} \right\rfloor > p \end{cases} \quad (30)$$

we see that for any given x_i , the ratio r_{gi} between the gradients in the outer and inner cases is $p(p - x_i/s) / (|x_i/s| - x_i/s)^2$. But since x_i recently switched cases, $(p - x_i/s) < 1$. As a rough estimate, we might expect $r_{gi} \approx (1/2p)/(1/12) \approx 6p$. Averaged over the entire input, $r_g \approx 6fp \lesssim p$. The $10\times$ over-design helps address some uncertainty in this measure as well.

B.1. Validation

Figure 9 shows a re-run of Figure 5 for the case of Adam optimization on log threshold gradients. These plots allow us to validate our Adam convergence analysis above. First we note that $p = 2^{8-1} - 1 = 127$, which is an approximate upper bound on r_g and well within the $10\times$ over-design principle. Next, notice that $T \approx r_g$. For example, in the $\sigma = 10^{-2}$ case, $T \approx 280$ while $r_g \approx 272$.

Most importantly, we expect the max log-threshold deviation to be upper-bounded by $\alpha \sqrt{r_g} = (1.6, 0.4, 0.7)$ from left to right if our original assumptions hold - that we visit

¹¹This is a problem when historical gradient magnitudes were higher, as is usually the case when $\Delta \lceil \log_2 t \rceil < 0$, as seen in the small σ plots of Figure 5.

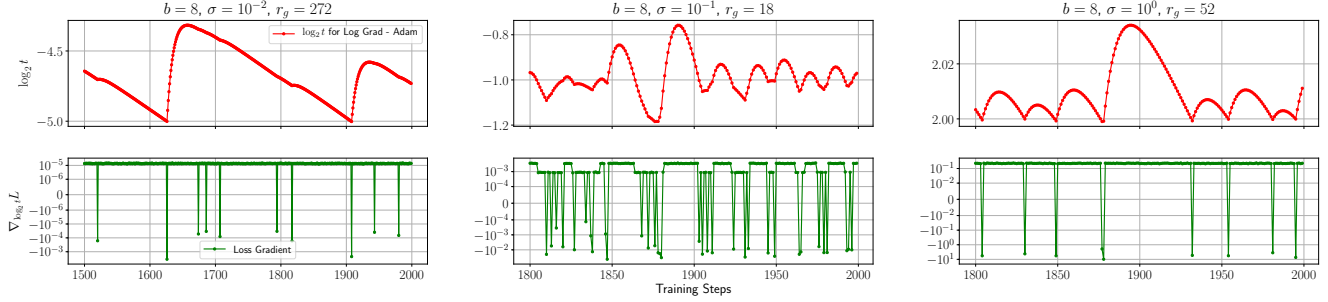


Figure 9. Close up of Figure 5 for the Adam-trained log threshold gradient on a few select settings.

the lower threshold bin for one step and stay in the upper bin for $T - 1$ steps. While the bound holds for all σ , it is close to not holding for $\sigma = 10^{-1}$. A brief inspection reveals why this is the case - the log threshold spends far more than one step in the lower threshold bin per period, violating our one-step assumption. This violation can be explained by looking at the gradients, which show that the lower threshold bin sometimes has positive gradients, depending on the randomness of the input Gaussian vector. These phenomena motivate our suggestion to over-design by $10\times$. The cost in additional steps needed to reach convergence seems like a worthwhile trade-off.